Degenerate Bose Fermi Mixture of Metastable Helium Atoms

Kieran F. Thomas,[1] Zhuoxian Ou,[1] Bryce M. Henson,[1] Angela
A. Baiju,[1] Sean S. Hodgmann,[1] and Andrew G. Truscott[1]

[1]*Department of Quantum Science and Technology, Research School of Physics,*
The Australian National University, Canberra, ACT 2601, Australia

We present a technique for achieving quantum degeneracy in both components of a Bose-Fermi mixture of metastable helium atoms, ^{3}He* and ^{4}He*. Degeneracy is achieved via Doppler cooling and forced evaporation for ^{4}He*, and sympathetically cooling ^{3}He* with ^{4}He*. We discuss our simplified implementation, along with the high versatility of our system. This technique is able to produce a degenerate Fermi gas with a minimum reduced temperature of $T/T_F = 0.14(1)$, consisting of 2.5×10^4 ^{3}He* atoms. Due to the high internal energy of both isotopes single atom detection is possible, opening the possibility of a large number of experiments into bose-fermi mixture which have thus far been inaccessible.

I. INTRODUCTION

The development of laser cooling techniques along with the application of evaporative cooling led to the first realization of Bose - Einstein condensation (BEC) in trapped atomic clouds in 1995 [1]. Since then BECs have provided a great range of experimental possibilities, such as atom optics [2–9], the study of the interaction between light and matter[10], and quantum computation [11, 12], as they offer a great degree of control and ease of measurement in a large quantum system. Like bosons, ultracold fermions also offer potential insights into numerous quantum phenomena, for example high temperature superconductivity [13], and fermionic superfluidity [14, 15], and have hence been an active field of experimental study in recent years [16–18]. Furthermore, degenerate bose-fermi mixtures have provided access to an even wider array of possible physics, such as phase separation [19–21], quantum droplets [22, 23], and polaron physics [24–27] .

While there have been a number of successful investigations into degenerate fermi gases and bose-fermi mixture [28–36], these investigations are generally less common compared to the pure bosonic counter parts. This is primarily due to the increased experimental complexity that fermionic gases bring, as the evaporative cooling that has allowed access to these ultracold temperatures is not directly applicable to fermions. Physically this limitation is caused by the vanishing of the fermi-fermi scattering cross section at low temperatures due to the Pauli exclusion principle, thus a requirement of evaporative cooling, rethermalisation, is not achieved (at least not over practical experimental time scales). To circumvent this issue the fermionic species is often cooled to degeneracy sympathetically with a bosonic partner species [37–39], as presented in this work.

Metastable helium (refreing to ^{4}He* or ^{3}He* in their respective 2^3S_1 excited electronic states) provides an especially unique platform for the study of dilute quantum gases due to its high internal energy, allowing for efficient single atom detection (for either isotope). In this project, we report on the production of a degenerate bose - fermion mixture of bosonic helium (^{4}He*) and fermionic helium (^{3}He*), in which after laser cooling the bosons are first cooled evaporatively and then used as a sympathetic coolant for fermions. The achievable temperatures relative to their respective critical temperatures and number of atoms, is presented and analysed. We describe our novel approach of modifying our existing apparatus for the cooling and trapping of ^{4}He* [40] to accommodate ^{3}He* with minimal alterations to the vacuum and laser system. This system is capable of demonstrating and studying many body correlations and could shed light on some of the most interesting problems in modern quantum physics.

II. BACKGROUND

In this section we will cover both the theoretical basis of the cooling techniques applied to ^{3}He and ^{4}He*, highlighting the most pertinent distinctions between the two species (arising primarily from differing electronic structures and masses).

A. Degeneracy Temperature for Bosonic and Fermionic matter

From their respective symmetries under particle exchange we find the behavior of bosons (symmetric) and fermions (anti-symmetric) are governed by Bose-Einstein statistics and Fermi-Dirac statistics respectively. The occupation probability $f(\varepsilon)$ for state with energy ε is,

$$f(\varepsilon) = \frac{1}{e^{\frac{\varepsilon - \mu}{k_B T}} + \delta} \tag{1}$$

where $\delta = 1$ for fermions, and $\delta = -1$ for bosons, μ is the chemical potential, k_B is the Boltzmann's constant and T is the absolute temperature. At high temperature, quantum statistics become negligible and both of these kinds of particles obey the classical Maxwell Boltzmann distribution $f(\varepsilon) \approx e^{-\left(\frac{\varepsilon - \mu}{k_B T}\right)}$.

However, below a certain critical temperature fermions and bosons displayed starkly different behaviour both

from one another and their classical counter parts. In our experiment the particles are confined in a harmonic trapping potential,

$$V_{f,b}(x,y,z) = \frac{m_{f,b}}{2}\left(\omega_x^{f,b}x^2 + \omega_y^{f,b}y^2 + \omega_z^{f,b}z^2\right) \quad (2)$$

where m_b is the mass of ^{4}He and $m_f = \frac{3}{4}m_b$ is the mass of ^{3}He. For the bosons, below the condensation temperature T_C, a macroscopic fraction of the total number of particles will occupy the lowest-energy single-particle statte, forming a Bose-Einstein condensate (BEC). If we have N_b bosons then the phase transition temperature T_c can be obtained as [41]

$$k_B T_C = 0.94 \, \hbar\bar{\omega}_b N_b^{1/3}. \quad (3)$$

where $\bar{\omega}_b = (\omega_x\omega_y\omega_z)^{1/3}$ is the geometric mean of the bosons' trapping frequencies.

In contract, for fermionic matter the Pauli exclusion principle prevents the simultaneous occupation of the exact same state by two fermions. As a consequence, at low temperature, every fermion settles into the lowest available energy state, successively filling them and forming a Fermi sea. The energy of the highest filled state is called the Fermi energy (E_F) and the corresponding temperature for this energy is the Fermi temperature $k_B T_F = E_F$. For a fermi gas containing N_f particles and with geometric average angular frequency $\bar{\omega}_f$ the total number of states with energy less than E is given by [41],

$$G(E) = \frac{1}{6}\left(\frac{E}{\hbar\bar{\omega}_f}\right)^3. \quad (4)$$

For a completely degenerate gas we have, $G(E_F) = N_F$ and thus we find an expression for T_F,

$$k_B T_F = (6N_f)^{1/3}\hbar\bar{\omega}_f. \quad (5)$$

We will refer to T/T_F and T/T_C as the reduced temperatures of the fermi and bose gases respectively. It is of relevance to note that for our experiment $\bar{\omega}_f = \sqrt{\frac{4}{3}}\bar{\omega}_b$ and hence $T_F = 2.23\left(\frac{N_f}{N_b}\right)^{1/3}T_C$.

B. Momentum and Time-of-Flight distributions

We will analyse our bose-fermi mixture by measuring the time of flight profiles of each species on an MCP delay line detector (as described in Sec. III B). In this section we will summarise the analytical forms of profiles for the BEC, DFG, and thermal component, the last of which will serve as our thermometer for the system. The distinctive profiles of ^{4}He* and ^{3}He* will also allow us to distinguish the species on the detector.

For large clouds of bosons the expression for the ground state distribution is given by Thomas-Fermi approximation, in which we ignore the kinetic energy of the atoms and assume interparticle interactions dominate. Under this approximation we can solve for the in-trap density profile of the BEC to be,

$$\rho_b(\vec{r}) = \begin{cases} \frac{\mu_b - V_b(\vec{r})}{g}, & \mu_b > V_b \\ 0, & \text{otherwise} \end{cases}$$

where μ_b is the boson chemical potential, and $g = \frac{4\pi\hbar^2 a_{44}}{m_b}$ is the interaction coefficient between bosons, with $a_{44} = 7.512(5)$ nm the ^{4}He*-^{4}He* scattering length [42]. For a harmonic confining potential this is the well know Thomas-Fermi inverted parabola profile. The time-of-flight expansions of a BEC has been investigated by Castin et al. [43], and was found to be well approximated by a rescaling of the in trap density profile. If we have a cylindrical trap $\omega_x \ll \omega_y, \omega_z$ and $\omega_y = \omega_z$, we can solve for the long time, $\omega_d t \gg 1$, time-of-flight profile of the BEC for a harmonic potential to be,

$$n_b^{tof}(x,y,z,t) = \begin{cases} \frac{\mu_b\left(1 - \sum_{d=x,y,z}\frac{r_d^2}{R_d(t)^2}\right)}{g}, & r_d < R_d \\ 0, & \text{otherwise} \end{cases}$$

$$(6)$$

where $R_{y,z}(t) = \sqrt{\frac{2\mu_b}{m_b}}t$ and $R_x(t) = \frac{\omega_x}{\omega_{y,z}}\frac{\pi}{2}\sqrt{\frac{2\mu_b}{m_b}}t$. Note that the time-of-flight profile of BEC does not ballistically map to its momentum profile [44], as is the case for the Fermi-Dirac and Maxwell-Boltzmann gases. Hence, generally the BEC profile alone does not encode any information on the temperature of the system.

To determine the density distribution of the trapped cloud of fermions we take the semiclassical approximation (also known as the Thomas-Fermi approximation) [45]. In this approximation each fermion is treated as having a definite position and momentum, and hence the many-body wavefunction is described by a semiclassical phase-space distribution $w(\vec{r}, \vec{p})$,

$$w(\vec{r}, \vec{p}) = \frac{1}{h^3}\frac{1}{\frac{1}{\xi}e^{\frac{H_f(\vec{r},\vec{p})}{k_B T}} + 1}, \quad (7)$$

where $H_f(\vec{r}, \vec{p}) = V_f(\vec{r}) + \frac{p^2}{2m_f}$ is the classical Hamiltonian for the fermions, and $\xi = e^{\frac{\mu_f}{k_B T}}$ is the fugacity. We neglect interactions between the fermions due to the suppression of s-wave scattering of identical fermions, and hence the ground state momentum density profile is given by an integral of w over position space [46]

$$n_f(p) = \frac{1}{(2\pi)^3}\int d^3\vec{r}\, w(\vec{r}, \vec{p}) \quad (8)$$

$$= -A_f \mathrm{Li}_{3/2}\left[-\xi \exp\left(-\frac{|\vec{p}|^2}{2m_f k_B T}\right)\right] \quad (9)$$

where $A_f = \frac{1}{(2\pi)^{3/2}\hbar^3}\left(\frac{k_B T}{m\bar{\omega}_f^2}\right)^{3/2}$, and Li_n is the polylogarithmic function of order n. Note that in the limit

of $T \to 0$ we obtain $n_f(\vec{p}) = \frac{8N_f}{\pi^2 (p_F)^3} \left[1 - \left(\frac{p}{p_F} \right)^2 \right]^{3/2}$ [45] where p_F is the Fermi momentum, $p_F = \sqrt{2mE_F}$.

The high momentum tails of both distribution are thermal, and are hence well approximated by a classical Maxwell Boltzmann distribution,

$$n_t(p) = A_t e^{-\frac{p^2}{2mk_B T}} \quad (10)$$

where $A_t = \frac{N_t}{(2\pi)^{3/2}(mk_B T)^{3/2}}$, for a given number of thermal particles N_t at a temperature T.

As we can neglect interactions in the fermionic and thermal components the momentum distribution can be converted to the far-field time-of-flight profiles using the procedure described in Yavin et al. [47]. To represent he coordinates of our measurement procedure we will assume our detector is along the $x-y$ plane, with the origin of the plane directly beneath the intial position of the cloud. Hence the coordinates (x, y, t) correspond to an atom arriving at the detector at time t at the spatial location (x, y) on the detector. First we transform the momenta (p_x, p_y, p_z) in to time of flight coordinate (x, y, t) via the equations for a ballistic motion under gravity,

$$(p_x, p_y, p_z) \mapsto m \times \left(\frac{x}{t}, \frac{y}{t}, \frac{g_0(t^2 - t_0^2)}{2t} \right) \quad (11)$$

where $t_0 = \sqrt{2l_0/g_0}$ is the fall time for a zero momentum particle, l_0 is the distance from center of cloud to detector, and g_0 is the acceleration due to gravity. We must also account for the change in differential volume between the two coordinate systems by multiplying the probability density by the relevant Jacobian $J = m_{f,b}^3 \frac{g_0 t^2 + 2l_0}{2t^4}$. Assuming the initial cloud can be treated as a point source, i.e. the spatial distribution can be ignored, the probability density distributions are related by

$$n^{tof}(x, y, t) = m_{f,b}^3 \frac{g_0 t^2 + 2l_0}{2t^4} n \left(\frac{x}{t}, \frac{y}{t}, \frac{g_0(t^2 - t_0^2)}{2t} \right), \quad (12)$$

where $n(p_x, p_y, p_z)$ is the corresponding in trap momentum distribution.

We cover the explicit details of fitting the experimental time-of-flight profiles, including accounting for interspecies mean-field effects and the shift in the center-of-momneumt of the clouds due to the separation magnetic pulse, in Appendix A. The momentum distributions, along with corresponding integrated time-of-flight profiles are displayed in Tab. I.

C. Laser trapping and cooling of ^{3}He* and ^{4}He*

To achieve quantum degeneracy in our Bose-Fermi mixture of He* atoms we apply a series of laser cooling and trapping techniques to both ^{4}He* and ^{3}He* simultaneously. Before using these techniques, we need to first produce metastable helium. However, optically producing He* by exciting helium from the ground state to the 2^3S_1 is impractical, as it would require far ultraviolet light which is not conveniently accessible, and furthermore the scattering cross-section of the transition is extremely small [48]. Therefore, we use high energy electron collisions in a discharge plasma to excite both species to the 2^3S_1 state. The 2^3S_1 state is a metastable state, with a lifetime of 7870(510) seconds [49], and can therefore be treated as an effective ground state. A high intensity beam of both species of He* is produced by a liquid nitrogen cooled DC discharge plasma source, with atoms in the correct state extracted via a deflector beam [50]. This beam is initially collimated by a 2-D optical molasses and slowed via a Zeeman slower, in which a red-detuned laser light combined with a magnetic field acts as a slowing force on the metastable atoms. A magneto-optic trap (MOT) then captures the slowed He* atoms [KT:what temp are both atoms at?]. After transferring the atoms from the MOT to a magnetic trap, 1-D Doppler cooling is employed to further cool the atoms [KT:what temp are the atoms at now] [40].

The laser cooling and trapping transitions employed in our experiment are the D_2: 2^3S_1 $(J=1)$ $\to 2^3P_2(J=2)$ transition for ^{4}He* and the C_3: $2^3S_1(F=3/2) \to 2^3P_2(F=5/2)$ transition for ^{3}He* respectively, as highlighted in Fig. 1 with the relevant electronic energy states. The Doppler limit of both of these transitions is $\sim 39\mu$K [51]. For efficient Doppler cooling we wish for the transitions to be recycling, i.e. on average they preserve the state of the atom after re-emission. According to the emission profile of the 2^3P_2 state [52], the metastable state is predominantly repopulated after re-emission, as the decay to the ground state is forbidden [?]. In the hyperfine structure of ^{3}He* $(I=1/2)$, the $F=5/2$ state can only decay to the $F=3/2$ metastable state following the selection rule. Therefore, both transitions are recycling. In the presence of a magnetic field, the recycling transitions for 1-D Doppler cooling are $m_J=1$ to $m_J=2$ in ^{4}He* and $m_F=3/2$ to $m_F=5/2$ in ^{3}He*, with a σ^+-polarized laser.

The frequency of the D_2 transition is 276.7322 THz (1083.331 nm) [53] and the frequency of the C_3 transition is 276.6986 THz (1083.462 nm) [54], thus the detuning between them is approximately 33.574 GHz [54]. This detuning is sufficiently large such that the laser for one transition will not cause any off-resonant excitation of the other transition. However, due to the small energy difference between the hyperfine states and the large natural linewidth $\Gamma=1.6$ MHz [55], the ^{3}He* laser frequency also induces strong off-resonant excitation from the metastable state to the $2^3P_2(F=3/2)$ state $(C_5$ transition), from which the atom decays to the 2^3S_1 $F=1/2$ state, causing a depletion of ^{3}He* in the $F=3/2$ metastable state. Meanwhile, as the detunings of the ^{3}He* laser with respect to the C_2 and C_4 transitions are -249Γ and 169Γ resepectively, the $F=3/2$ metastable state can be frequently repopulated by the decay from
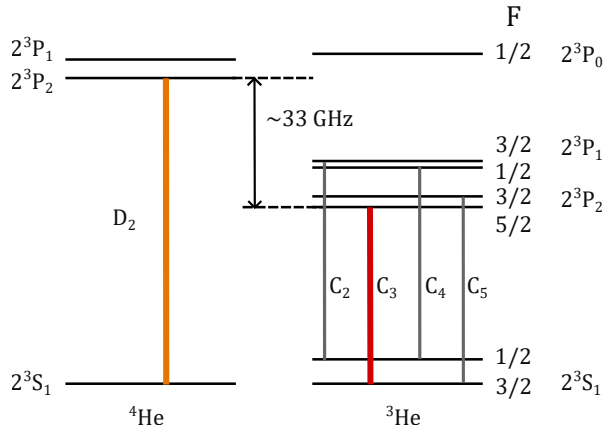
FIG. 1. Energy level diagrams of metastable ^{4}He* and ^{3}He*. The spacing of energy levels is only indicative. The 2^3S$_1$ state has a lifetime of 7870(510) seconds [49]. The D_2 and C_3 atomic transitions for laser cooling and trapping are indicated in yellow and red respectively. The resonant frequencies of these two transitions are 276.7322 THz (1083.331 nm) [53] and 276.6986 THz (1083.462 nm) [54]. Off-resonant excitation of the C_5 transition can be induced by the C_3 frequency, which is 1.781 GHz below the C_3 frequency [54]. However, the C_2 and C_4 act as repumpers to repopulate the F=3/2 metastable state [56].

the 2^3P$_2$(F=1/2) and 2^3P$_1$(F=3/2) states [56]. Therefore, this leakage is strongly suppressed and a repumper is not required to excite atoms out of the dark ground state for any stage.

D. Evaporative and Sympathetic Cooling

For our system laser cooling alone is not enough to reach quantum degenerate temperatures. To achieve degeneracy we apply radio-frequency (RF) induced forced evaporation in a magnetic trap. In this process RF ~~light~~ is applied to the mixture, which is tuned close to the level splitting between the $m_J = +1$ and $m_J = 0$ 2^3S_1 states of the ^{4}He* gas. The frequency is blue detuned ~~of the transitions~~, such that ~~the~~ more energetic atoms are most likely to absorb a photon, and hence be expelled from the magnetic trap. The resulting gas ~~hence~~ has a lower average energy per atom and thus a lower temperature. The frequency is then slowly lowered, progressively removing lower energies. We characterise the evaporation cycle by the detuning, or height, of the final frequency applied from the frequency of the transition for an atom at zero temperature. This is equivleant to the detuning for an atom sitting at the minimum of the trapping potential, thus we refer to this parameter as the evaporation height above trap bottom.

While we have successfully applied this technique to ^{4}He* to achieve BEC [40] it can not be directly applied

to ~~the~~ fermionic ^{3}He*. ~~It is well know from scattering theory that~~ only the s-wave component of a potential has a nonzero contribution to the scattering amplitude in the low energy limit. However, due to the Pauli exclusion principle the s-wave scattering length of fermions is zero, and thus a fermi gas will be unable to rethermalise with itself via elastic collisions [57]. However, as the fermions are in thermal contact with the bosons and the interspecies scattering length is ~~non-zero~~ $a_{34} = 29(4)$ nm [39], then for sufficiently slow evaporation the fermions will remain in thermal equilibrium with bosons as they are cooled. Given that the expected interspecies scattering length is significantly higher than the intraspecies scattering length ~~of ^{4}He*~~ $a_{44} = 7.512(5)$ nm we were able to use the same evaporation cycle that is used for a pure sample of ^{4}He* (approximately 16 s in length). The change in temperature of the mixture due to the forced evaporation process depends on the efficiency of the evaporation ramp (parameterised by η), the sum of the heat capacities, and the rate of change in energy of the bose gas with respect to particle number [58]. As the behaviour of the thermodynamic properties of the gases change between the classical and degenerate regimes, especially for a bose gas, the exact behaviour is fairly complex. However, if the heat capacity of the fermi gas is negligible compared to the heat capacity of the bose gas for all temperatures greater than T_C, then the final reduced temperature of the fermi gas T/T_F is only dependent on the ratio N_b/N_f, where N_b and N_f are the number of bosons and fermis in the mixture after evaporation [59]. This implies that having a larger initial number of fermions is equivalent to evaporating closer to the trap bottom (the detuning for zero momentum), in terms of the reduced temperature reached. Furthermore, as T_F and T_C are related ~~by $T_F = 2.23 \left(\frac{N_f}{N_b} \right)^{1/3} T_C$~~ and the mixture is in thermal equilibrium the reduced temperature of the bose gas will also only depend on the ratio N_b/N_f. This also implies for a given evaporation efficiency and initial phase space density there is an optimal Fermi reduced temperature that can be reached (i.e. when all the coolant, ^{4}He* gas, has been used up).

Furthermore, if ^{3}He* is in thermal equilibrium with ^{4}He* then the energy of an ^{3}He* atom resonant with a given evaporator height will be higher than that of a ^{4}He* atom. Thus a negligible amount ^{3}He* is removed in the evaporation process. Note that once all ^{4}He* atoms have been evaporated, if we continue to lower the evaporator height then ^{3}He* atoms will be removed.

III. APPARATUS

In this section we will cover the technical aspects of our experimental apparatus, focusing on the modification required to incorporate ^{3}He* into the cooling process, specifically the laser and vacuum system.

A. Magnetic Trap

We perform our 1D Doppler cooling and RF evaporation of the two species in a biplanar quadrupole Ioffe magnetic trap [40], which can be treated as a harmonic with cylindrical symmetry. For the data presented in this work we have used trapping frequencies $\{\omega_x, \omega_y, \omega_z\}/2\pi \sim \{60, 600, 600\}$ Hz, with gravity aligned along the z-axis. The trapping frequencies were measured using a pulsed atom laser technique described in Ref. [60].

B. Detection

We measure the far-field time of flight profiles for both species using micro-channel plate and delay line detector (DLD) [5] system, which due to the high internal energy of both species metastable state allows us to detect the positions of single atom impacts after they are released from the trap. The MCP is located 858.7 mm below the trap, which corresponds to a fall time of $t_0 = 0.4187$ s, for a particle with zero initial momentum.

As both clouds momenta distributions are initially centered on zero they will overlap on the detector if they are only influenced by gravity. To separate the clouds we apply a linear magnetic field gradient to both species, produced by a set of coils surrounding our BEC chamber. While the two isotopes have the same magnetic moment, and hence experiences the same force from the external field, they will be accelerated different amounts due to their differing masses. This pulse alters our time of flight profiles and must be accounted for in order to get accurate measurements of the mixtures properties, see Sec. II B.

Our detector saturates at flux rates greater than 500 kHz, which is much lower than the peak rates of our ultracold clouds and hence underestimating their true atom number. To circumvent this issue we employ a pulsed atom laser technique for $^4\text{He}^*$ [60], which out couples only small portions ($\sim 2\%$) of the cloud, with each pulse being well below the saturation limit and thus giving an accurate measure of the $^4\text{He}^*$ atom number. In order to determine the atom number of the $^3\text{He}^*$ cloud we employ absorption imaging. In this procedure probe light resonant to an atomic transition is shone through the cloud and compared to a reference image of no atoms, to determined the amount of light absorbed. The change in intensity due to an absorption medium is governed by Lambert Beer's law [61], which for a sufficiently low intensity probe beam can be solved to give

$$D(x,y) = \sigma_a \int \rho(x,y,z)dz \tag{13}$$

where the optical density D is defined as $I_{\text{out}} = I_{\text{in}}e^{-D}$ and the absorption cross section σ_a is given by

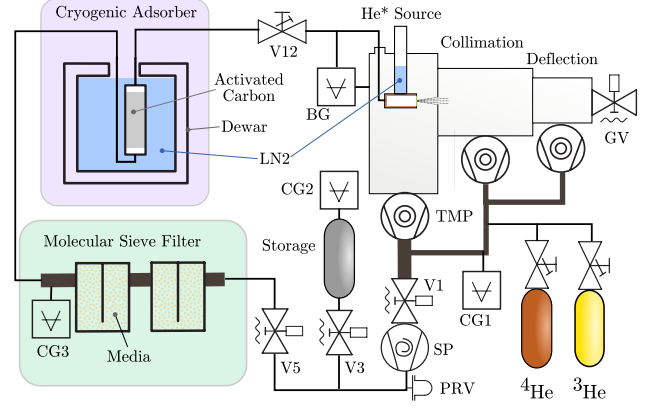$$\sigma_a = \hbar\omega \frac{\Gamma}{2I'_{sat}} \frac{1}{1 + I/I'_{sat}}. \tag{14}$$

FIG. 2. Simplified schematic of recycling system. Abbreviations: TMP - Turbomolecular Pump, SP - Scroll Pump, PRV - Pressure Release Valve, BG - Baratron Gauge, LN2 - Liquid Nitrogen, GV - Gate Valve

The effective saturation intensity is given by $I'_{sat} = fI_{sat}/\chi$ where $I_{sat} = \frac{\hbar\omega^3\Gamma}{12\pi c^2}$ for a two-level transition with natural linewidth Γ and transition energy $\hbar\omega$, χ is the line shape factor, and f describes the distribution over the magnetic substates [61]. Strictly speaking, the above relations Eqns. 13 and 14 are only valid for $I \ll I'_{sat}$. For negligible temperature and laser linewidth χ is defined purely by the detuning Δ from the transition and the transition width,

$$\chi(\Delta) = \frac{1}{1 + (2\frac{\Delta}{\Gamma})^2}. \tag{15}$$

We image an initially unpolarised sample, however the linear polarisation of our probe beam will pump the atoms into a steady state after some time (approximately 50 μs for our experiment). Using the relevant Clebsch-Gordan coefficients we can solve for the steady state distribution and find $f = 25/14$ for $^3\text{He}^*$. Hence, we can find the number of $^3\text{He}^*$ atoms in our mixture via the relation $N_f = \frac{1}{\sigma_a} \iint dxdy\, D(x,y)$

C. Recirculation system

To produce a beam of He* in our experiment we use a DC plasma discharge combined with a supersonic expansion into vacuum. This process is relatively inefficient with proportion of about 10^{-8} of the atoms converted into He* making it into the first stage of the system (collimator). The remaining gas is pumped away with a turbo molecular pump and previously had been eventually discharged to atmosphere.

While this approach is reasonable with ^4He which is relatively inexpensive the cost of ^3He can quickly become prohibitive. To produce meaningful results we therefore have to find a means to reduce this prohibitive cost.

~~While a decrease of in consumption of approximately 10 could be a achieved buy only running the source in the first few seconds of an experiment when the first MOT is loaded this is still beyond our budget for all but the most simple experiments. Instead we implement a~~ system that can recycle the helium gases used in the experiment.

To recycle the gas requires compressing the gas that is captured by the three relevant vacuum pumps (see Fig. 2), to the ~~source~~ pressure (between 10 and 0.5 kPa) and then feeding it back into the source. ~~Further more~~ the source is very sensitive to contaminants, particularly organics ~~which~~ are decomposed by the source into carbon soot and oxygen which erodes the copper and tungsten. In the previous system contaminates were avoided by using high purity helium gas, however in the recycling system oil ~~in~~ vacuum pumps and the inevitable leakage of air into the system will build up and must be dealt with.

To reduce the source of oil as much as possible we replace the rotary-vane backing pump for the source turbo, which uses oil as a sealing and lubricating agent, with a 'dry'(oil-free) scroll pump. This does not eliminate oil from the system entirely as all three of the turbomolecular pumps use oil lubrication of the rear bearing. To manage this contamination two filter stages are used. First on the backing line of the turbomolecular pumps we use micromaze traps ~~which contain~~ a number of highly porous ceramic plates ~~which traps~~ oil vapour. This serves to reduce the contamination of the scroll pump which compresses the gas to the source pressure. After compression the gas then passes through two molecular sieve filters filled with SSZ-13 zeolite media. This second stage further reduces oil and presents a large surface area which also serves to adsorb water vapour. The molecular sieves can be partially regenerated by removing the circulating gas and heating them to approximately 120° C.

As the recycling system is closed any small air leaks will compound over time. To remove this air the final filtration stage uses a liquid nitrogen cooled activated carbon adsorber. At low temperatures gas molecules make a weak van-der walls bond to the carbon (adsorption), and the high surface area of activated carbon improves the total absorption capacity. By operating at liquid nitrogen temperatures the absorption of helium is negligible. ~~The adsorber is kept at this temperature by placing it inside a large (100 L) liquid nitrogen dewar which keeps the adsorber submerged for weeks between liquid nitrogen transfers.~~ This stage is able to remove all atmospheric gases (oxygen, nitrogen, water). To regenerate the adsorber the liquid nitrogen is removed from the dewar and the unit heated to approx 120° C ~~using resistance wire wrapped around the outside~~. During regneration of the adsorber and the molecular sieves the helium gas is stored in a separate storage tank. ~~The system is then pumped to atmosphere with a secondary scroll pump.~~

A key parameter for engineering this system is the amount of ^{3}He needed to fill the system. This is set by the volume (tubing and filters) which is pressurised
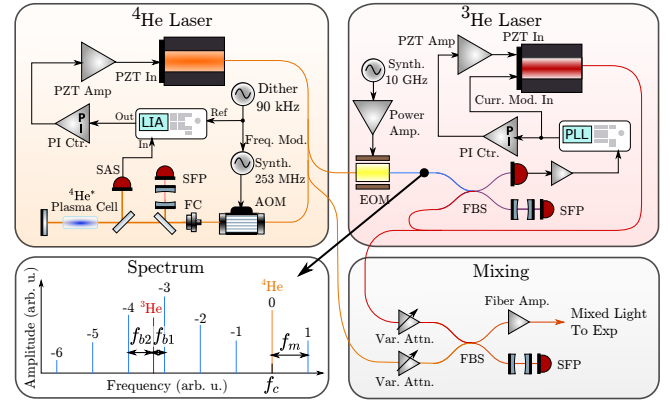

FIG. 3. Laser system. Abbreviations: AOM - Acousto-Optic Modulator, EOM - Electro-Optic Modulator, Var. Attn. - Electronical Variable Optical Attenuator, PZT - Piezoelectric Actuator, Curr. Mod - Current Modulation, Freq. Mod. - Frequency Modulation, Synth. - RF Synthesizer, PI Ctr. - Proportional Integral Controller, SAS - Saturation Absorbtion Spectroscopy, FBS - Fiber Beamsplitter, SFP - Scanning Fabry-Perot Interferometer. Spectrum For modulation of 4.4 rad. 3rd sideband amplitude is 0.22. f_{b1} and f_{b2} are the lowest frequency beatnotes produced when the ^{3}He laser is mixed with the frequency comb.

to the ~~source pressure and~~ the pressure required to start the plasma. ~~To operate the plasma source the flow of helium is turned up using the flow control vale in order to initiate a plasma and is then decreased to maximize the metastable flux.~~ This pressure decreased to a few kPa by using a flyback based high voltage ignition system from a residential babeque. ~~By carefull design of the filters~~ the total volume at the source pressure is kept to 5 L. The total gas need to operate the system is then 0.1 L STP which in a 50:50 ratio of ^{3}He to ^{4}He represents a few hundred AUD of ^{3}He.

The recycling system only captures gas before the Zeeman slower however ~~both the~~ helium background ($1 \cdot 10^{-2}$ L STP/year) and metastable flux ($2 \cdot 10^{-4}$ L STP/year) losses are ~~sufficiently~~ small. ~~This was chosen to keep the system smaller reducing oil contamination and to isolate the vacuum systems across the Zeeman slower gate valve for ease of maintenance.~~

As a test of operation ^{4}He has been successfully recirculated for months at a time without problem. A residual gas analyser fixed to the the collimator stage was used monitor the gas composition of the source with no detectable impurities above the background levels in the chamber.

D. Laser lock

A laser with a stable frequency is important for cooling and trapping an atomic gas. In our setup an external-cavity laser (ECL) system is used for ^{4}He* [62], featuring a diffraction grating that selects the laser wavelength.

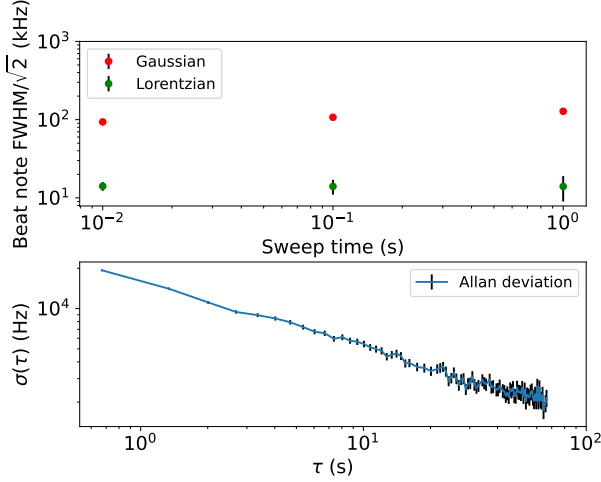FIG. 4. The first graph shows the FWHM/$\sqrt{2}$ of both the Gaussian and Lorentzian of the locked beat note for different sweep times. As the sweep time increases, the beat note linewidth given by the Gaussian shows a slightly increasing trend while the linewidth estimated by the Lorentzian remains to be stable. The beat note is estimated to have a linewidth of ∼100 kHz. The second graph shows the Allan deviation $\sigma(\tau)$ of the beat note frequency. It decreases over time as the noise of the signal measured at different times cancels out.

The grating is installed on a piezoelectric chip (PZT) that controls the angle of the grating and finely modulates the wavelength. This ECL is locked to 1083.331(1)nm using saturated absorption spectroscopy (SAS) [62]. For He* , due to the need to have an excited state population, SAS requires an RF discharge driven plasma inside the vapour cell as an atomic reference. Due to problems caused by the plasma etching, the cell needs to be refilled regularly. However, the high cost of ^{3}He* means we utilized an alternative setup to stabilize the laser for cooling and trapping of ^{3}He*. Instead, we have developed a laser locking scheme that uses frequency combs and a phase-locked loop, to lock the ^{3}He* laser relative to the ^{4}He* laser by stabilizing the beat frequency between the two lasers (see Fig. 3).

As discussed in Sec. II C the ^{3}He* laser needs to be locked to the C_3 transition ($2^3S_1(F = 3/2) \rightarrow 2^3P_2(F = 5/2)$), which is 33.574 GHz red detuned from the ^{4}He* D_2 transition ($2^3S_1 \rightarrow 2^3P_2$). This can be achieved by using a high frequency optical phase modulator to add sidebands onto some of the ^{4}He* laser light, effectively making a small span frequency comb. The ^{4}He* laser is sent through an NIR-MPX-LN-10 electro-optic modulator (EOM) by iXblue Photonics, driven by a 10 GHz RF frequency synthesizer (Windfreak SynthHD v2) and amplifier (Mini Circuits ZVE-3W-183+). This procedure is illustrated in Fig. 3, which also shows an indicative spectrum of the ^{4}He* laser (in orange) as the carrier frequency

f_c and its sidebands (in blue) up to 6th order. The modulation frequency f_m is set by the Windfreak generator and the N-th order sideband has the frequency $f_c \pm N f_m$. The ^{3}He* laser and the ^{4}He* laser with its sidebands are mixed on a photodiode, which generates a series of beat frequencies equal to the aboslute value of the offset between the ^{3}He* laser and the sidebands. Although the detuning between the two lasers is ∼ 33 GHz, the beat signal between the ^{3}He* laser and the sidebands can be reduced to ∼1 GHz or even lower, which can be easily observed on a spectrum analyzer after being sent through a Fabry-Perot cavity.

The ^{3}He* laser is stabilized by a feedback loop that compares a chosen beat frequency with a reference and generates an error signal to tune the PZT of the ^{3}He* laser. The beat note between the 3rd-order sideband (denoted by "3" in Fig. 3) and the ^{3}He* laser has a frequency f_{b1}, which is typically ∼1 GHz when the RF driving frequency is approximately 10 GHz. f_{b1} is divided and compared with a 10 MHz frequency generator (Trimble, TPN: 57964-80 synchronous clock board) by an LTC6947 Fractional-N Synthesizer (Linear Technology). The LTC6947 board outputs a charge pump current that is proportional to the frequency difference between f_{b1} and the target frequency of this beat note. A transimpedance amplifier converts this current into an electric voltage, which serves as the error signal. The error voltage is integrated by a proportional-integral controller and is sent back to the PZT of the ^{3}He* laser to tune the laser to the required frequency (see Fig. 3)

The linewidth of the beat note is one of the indicators of the performance of the laser lock. To evaluate the linewidth, a Gaussian is fitted to the central region that spans for ≈1 MHz of its spectrum and a Lorentzian is fitted to the tails [63, 64]. The beat signal linewidth is bounded by the FWHM/$\sqrt{2}$ of the Gaussian and the FWHM/$\sqrt{2}$ of the Lorentzian, where FWHM is full width at half maximum. Figure 4 shows the linewidths measured for a series of sweep times of the spectral analyzer. The linewidth is deduced to be on the order of 100 kHz, which is much smaller than the natural linewidth of the relevant transitions, $\Gamma = 1.6$ MHz. In Fig. 4 we also show the Allan deviation measured for an hour, with a sample frequency of ∼1.5 Hz. The decreasing trend implies that the noise of the laser system cancels out over time. As the Windfreak synthesizer can output a frequency up to 15 GHz and the LTC6947 board has been shown to be able to lock a 1 GHz input signal, in principle this laser locking scheme can stabilize a frequency offset up to 46 GHz between two lasers, by locking one laser to the 3rd-order sideband of the other laser. This span could be improved further by using higher order sidebands, though this would require more power for the locking scheme due to the diffraction efficiency decreasing with higher order.

To incorporate the ^{3}He* light into the ^{4}He* BEC experimental apparatus [40] requires overlapping the ^{3}He*

laser with the ^{4}He* laser for every atom-optic element of the apparatus. The ^{4}He* laser has been amplified by a fibre amplifier (Nufern, NUA-1064-PB-0005-A2 fiber optic amplifier) before it enters the apparatus, we mix the ^{3}He* laser with the ^{4}He seed light with a 50:50 beam splitter, then inject it into the amplifier. The output of the amplifier now contains both frequencies of light, and they are hence overlapped in the atom-optic elements previously arranged for the ^{4}He* laser. This avoids duplicating many of the optical component of ^{3}He*. The ratio of power of the frequencies produced by the amplifier is very stable and equal to the ratio of power present in the seed light. Variable attenuators are applied to both lasers to dynamically control the ratio of light into the fibre amplifier and the apparatus. Using this method, the ^{3}He* laser is introduced into the apparatus without extra alignment of optics but with an adjustable power ratio and frequency. This also means that both lasers are sent through the same acoustic-optic modulators (AOMs) that control the laser detuning at each laser cooling and trapping stage. Therefore, the same detuning is applied to both frequencies with respect to their corresponding resonance. The ability to independently control the detuning of each laser via the AOM is compromised for the simplicity and convenience of overlapping the two lasers using the fibre amplifier. As we only need to sympathetically cool a limited amount of ^{3}He [58], this compromise only leads to a minimal decrease from the optimal conditions that would be possible with independent optics for each laser.

IV. RESULTS

In this section we will discuss the level of degeneracy achieved in our bose-fermi mixture, along with how our main two control parameters, detuning of the ^{3}He* laser and evaporator height, affect the most relevant experimental parameters, reduced temperature and atom number of the respective gases.

A. Time-of-flight profiles

We find temperature of the final mixture from the high momentum tails of the time-of-flight profile of the ^{4}He* atoms (see Fig. 5). This is because the Fermi-Dirac distribution approaches a thermal Maxwell-Boltzmann more slowly compare to a Bose-Einstein distribution. Furthermore, it is difficult to accurately fit the temperature and fugacity of Fermi-Dirac distribution independently as there is strong cross correlation between their values. See Appendix A for details on fitting procedure and derivation of uncertainty in the temperature measurement. However, we still fit the Fermi-Dirac distribution as a verification of the order of magnitude of the temperature measurement of the ^{4}He* cloud.

An important condition for our data analysis is hence

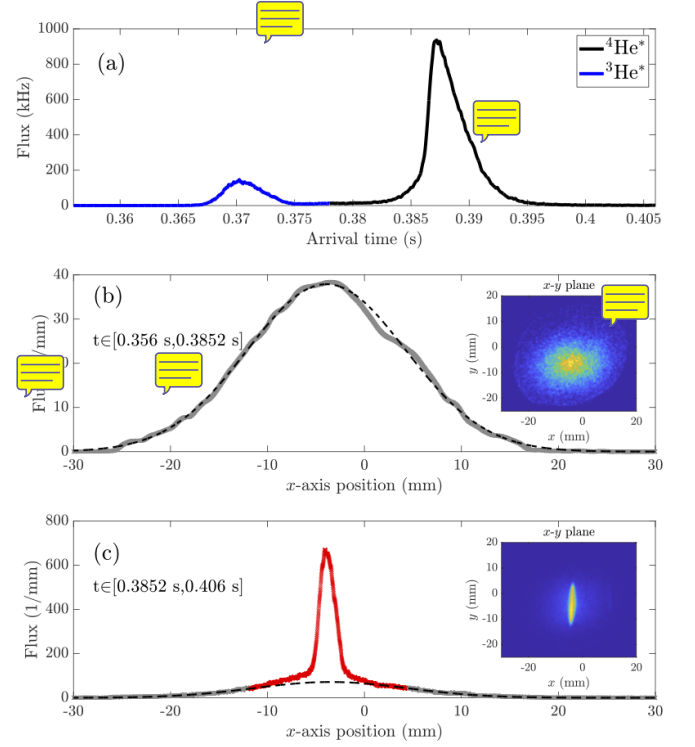FIG. 5. Time-of-flight profiles for ^{3}He* and ^{4}He* for evaporation height 15 kHz and detuning $\Delta = 1.0$ MHz . ~~For our system the detector is ~ 850 mm below the trap, with a diameter of ~ 80 mm.~~ (a) We show the flux as a function of arrival time after trap switch off. The two species are separated in time by a magnetic field gradient. The ^{3}He* cloud lands on the detector first with its center arriving at 0.377 s after trap switch off and is highlighted in blue, while the center of the ^{4}He* cloud arrives at 0.387 s after trap switch off. (b) Average x-axis flux of the ^{3}He* cloud (for arrival time between [0.356 s, 0.3852 s]) fitted with a Fermi-Dirac distribution with $T = 174(10)$ nK, and $\xi = 3.8(2)$ (black dashed line). Inset shows the density distribution over the x-y plane, demonstrating the isotropy of the cloud. (c) Average x-axis flux of the ^{4}He* cloud (for arrival time between [0.3852 s, 0.406 s]). We fit a thermal distribution (black dashed line) with $T = 215(18)$ nK to the wings of the distribution, coloured in gray, removing the central area which is either overlapped with the condensate or affected by its mean-field, coloured in red. This corresponds to a reduced temperature of $T/T_F = 0.56(4)$ for the fermions. Inset shows the density distribution over the x-y plane, demonstrating the anisotropy of the BEC.

that both gases are in thermal equilibrium at the time of release from the trap. Due to the high scattering length between the species $a_{34} = 29(4)$ nm we expect them to thermalise relatively quickly, however due to the difficulty of extracting the temperature from the Fermi distribution accurately we cannot confirm this directly. ~~For thoroughness~~ in the data presented here we hold the clouds for 400 ms after the end of evaporation~~, to ensure they have thermalised~~.

B. Dependence on laser detuning and evaporator height

As the same relative detuning an optical path is employed for both $^3\text{He}^*$ and $^4\text{He}^*$ for all cooling we are effectively only able to change the initial amount of $^3\text{He}^*$ in our final magnetic trap via three methods: the ratio of the amount of ^3He and ^4He gas in the metastable source; the ratio of power between ^3He and ^4He light (controlled by changing the ratio of power in the seed light); and the detuning of the ^3He seed light from its cooling transition, which can be controlled independently of the detuning of the ^4He seed light. For this work we only focus on the behaviour of ^3He detuning as it is the only parameter of the three, which changes the initial amount of $^3\text{He}^*$ atoms, while leaving the initial amount and temperature of $^4\text{He}^*$ atoms completely unchanged. All relative detuning and alignment of optomechanical components are optimised for ^4He flux. As will be shown this is reasonable as even with suboptimal conditions for $^3\text{He}^*$ we can still load more $^3\text{He}^*$ into the magnetic trap than we can effectively cool [58]. In Fig. 6 we show how the atom numbers, temperature, and reduced temperatures vary with ^3He detuning for a fixed evaporator height of 15 kHz. It can be seen there is a region around resonance were all $^4\text{He}^*$ atoms are evaporated. We do not present a temperature measurement in this region due to the unreliability of the temperature measurement from the fermic cloud. In this data set we have a minimum boson reduced temperature of $T/T_C = 0.25(1)$. Note that our system is capable of achieving significantly lower reduced temperatures of the boson cloud, however we wish to keep a significant portion of the $^4\text{He}^*$ cloud thermal in order to more easily measure the temperature.

In Fig. 7 we investigate the effect of evaporator height on the mixture's reduced temperatures and atom number. As expected the mixtures temperature and $^4\text{He}^*$ atom number decrease with evaporator height, while the $^3\text{He}^*$ atom number remains roughly constant until almost all $^4\text{He}^*$ atoms have been evaporated. The fermi reduced temperature hence decreases with evaporator height, while the bose reduced temperature increases when then is a non-zero number of $^3\text{He}^*$ atoms.

As discussed in Sec. II D the behaviour of the reduced temperatures seen in Figs. 6 and 7 can be understood purely by how each variable (detuning of $^3\text{He}^*$ laser and final evaporator height) effect the ratio N_b/N_f. In Fig. 8 we show how the bose and fermi reduced temperatures T/T_C and T/T_F vary with the atom number ratio N_b/N_f. We find that the fermi reduced temperature follows the expected relation derived from comparing heat capacities of the coolant ($^4\text{He}^*$) to the atom being sympathetically cooled ($^3\text{He}^*$), and modeling the forced evaporation as a temperature dependant energy cutoff [58, 59]. For our system we have that the bose and fermi critical temperatures are related purely via the atom number ratio,
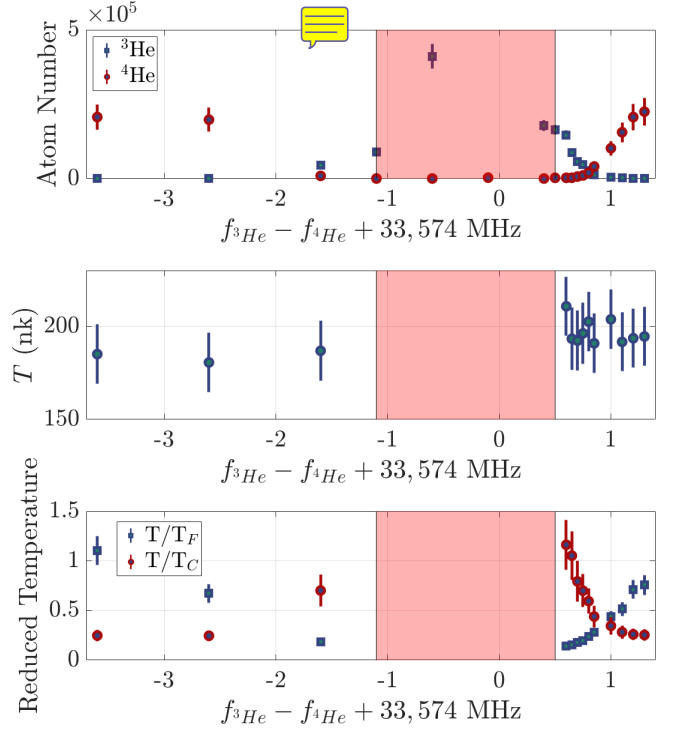

FIG. 6. Atom numbers of both species and temperature of mixture against the detuning of the $^3\text{He}^*$ laser from the cooling transition for a fixed evaporator height of 15 kHz. This allows us to effectively load in various amounts of ^3He atoms into the trap, while leaving the initial number and temperature of the ^4He atoms unchanged. The region with no ^4He atoms is shaded red. We do not present temperature measurements in this region as our temperature measure from the Fermi cloud is unreliable, as described above.

$T_F = 2.23 \left(\frac{N_f}{N_b}\right)^{1/3} T_C$. Thus we can convert the relation between the fermi reduced temperature and the atom number ratio to a relation for the bose reduced temperature.

It is interesting to note that this relation holds regardless of the method via which these parameters are changed. This implies an optimal fermi reduced temperature for our current experimental conditions of $T/T_F = 0.18(3)$, in the limit of complete evaporation of $^4\text{He}^*$. This compares well to the minimum experimentally observed reduced temperature of $T/T_F = 0.14(1)$, achieved for an evaporator height of 15 kHz and detuning of -1.6 MHz. We note that this value is well into the quantum degenerate regime. If instead we wish to produce a highly degenerate mixture we can optimise this degeneracy by finding the minimum of the average of the bose and fermi reduced temperatures. We have a theoretical optima of $T/T_C = 0.32(1)$ and $T/T_F = 0.24(1)$ at $N_b/N_f = 5(2)$. We achieve an experimental minimum for an evaporator height of 10 kHz and detuning of 0.75 MHz giving atom number ratio $N_b/N_f = 3.0(4)$ and reduced temperatures $T/T_C = 0.31(4)$ and $T/T_F = 0.20(3)$.
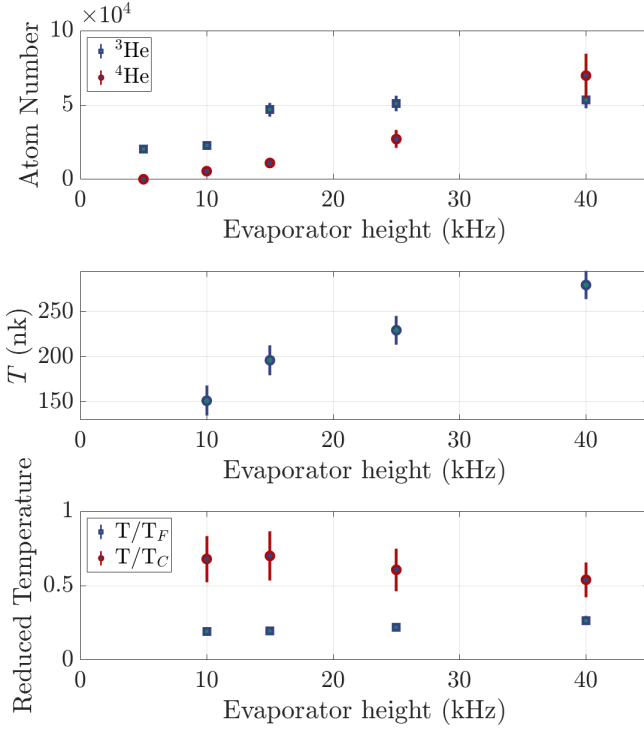
FIG. 7. Atom numbers and reduced temperature versus the final height of the forced evaporation above the trap bottom, for a fixed ^{3}He* detuning of 0.75 MHz. Note that the ^{3}He* number remains unchanged until almost all of the ^{4}He* have been evaporated, as expected. Furthermore, we see that while the temperature of the mixture decreases with evaporator height, the reduced temperatures remain roughly, with a slight reduction in T/T_F.
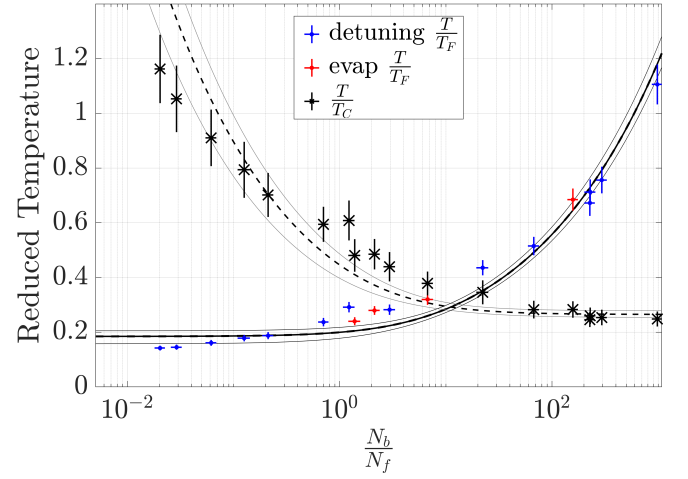

FIG. 8. The reduced temperatures T/T_F and T/T_C against the ratio of the number of bosons to fermions after the evaporation cycle. We see that T/T_F and N_b/N_f are equivalently related (solid line) for small changes to either the initial number of fermions (blue points) or evaporator height (red points) [59]. This implies an optimal fermionic reduced temperature of $T/T_F = 0.18(3)$, which compares well to our experimentally observed optimal reduced temperature of $T/T_F = 0.14(1)$. Using the relation $T_F = 2.23 \left(\frac{N_f}{N_b} \right)^{1/3} T_C$ we can T/T_F dependence on N_b/N_f (dashed line). The minimum of the average reduced temperature of both species is achieved for $T/T_C = 0.31(4)$ and $T/T_F = 0.20(3)$ with $N_b/N_f = 3.0(4)$.

V. CONCLUSION

In this work we have successfully produced a degenerate Fermi gas of ^{3}He* with a minimum reduced temperature of $T/T_F = 0.14(1)$, via sympathetic cooling with ^{4}He* that is under going forced evaporation. This limit could be improve further by using dynamic control of the relative intensity of the two frequencies of light, such that it is optimised for each stage of the experiment. This is especially relevant for 1D Doppler cooling employed to initially cool both species, as this stage has a very strong effect on the initial phase space density of the mixture. This limit can also be improved simply by increasing the heat capacity of the initial ^{4}He* sample.

This technique can serve as an excellent platform for a range of possible experiments in the areas of many-body physics, quantum atom optics, and bose-fermi mixtures. One pertinent example is the measurement of the ^{3}He*-^{4}He* s-wave scattering length a_{34} experimentally for the first time. The capability of single particle detection for ^{3}He* also provides the opportunity to measure many-body correlations that display higher order antibunching [], which has so far been unobserved. This is behaviour is the equivalent Hanbury Brown-Twiss effect for fermions,

which has been used to experimentally observe higher order bunching in bosonic ^{4}He* atoms [65, 66], and second order (two-body) antibunching in fermionic ^{3}He* [2]. It also allows access to interesting many body phenomena, such as s-wave scattering between a highly degenerate BEC and DFG, which will have a different mixture of bose bunching and fermi antibunching depending on the number of particles from each source being scattered.

Furthermore this s-wave scattering can be used to obtain a momentum entangled state of ^{3}He* and ^{4}He*. As the different atomic species have different masses, and hence could be used in a differential gravitational acceleration measurement, this state could be used to test the validity of the weak equivalence principle for a nonclassical state [67]. While the weak equivalence principle has been extensively tested in the classical regime, its validity for quantum entities is still an open question. Hence such a test would constitute a major step in the exploration of quantum gravitational phenomena.

Finally this system could also be used to continue our spectroscopic investigation of the atomic structure of helium, allowing us to observe thus far unseen quantum electrodynamic effects [10].

Appendix A: Fitting time-of-flight profiles

In this section we will detail how we fit the time-of-flight profiles in order to extract our temperature measurement. We are able to derive the expected time-of-flight profiles from the procedure described in Sec. II B. To simplify the fitting process we integrate out two of the time-of-flight dimensions. Explicitly this can be written as

$$n_f^{tof}(t) = \int_{-\infty}^{\infty} \int_{-\infty}^{\infty} dx\, dy\, n_f^{tof}(x,y,t) \qquad (A1)$$

$$n_f^{tof}(x) = \int_{0}^{\infty} dt \int_{-\infty}^{\infty} dy\, n_f^{tof}(x,y,t) \qquad (A2)$$

We summarise the relevant momentum distributions and integrated time-of-flight profiles for a BEC, DFG, and thermal gas, in Tab. I. For this work we extract the temperature by fitting a thermal distribution to the high momentum tails of the x-axis of the integrated time-of-flight profile of the ${}^4\text{He}^*$ cloud. This is because while the central region of the momentum distribution consists of a BEC, momentum significantly higher than the radius of the BEC can still be treated as thermal, and thus contain temperature information. We fit along the x-axis as this in the axis in which the BEC has the smallest momentum width, equivalently this is the weakest axis of the trap. In the other axes there is a significant overlap between the BEC and thermal components, i.e. their widths are of comparable values.

In order to determine that we are fitting sufficiently high in the momentum tails we repeat our thermal fitting procedure while removing increasingly larger portions of the cloud's center, see Fig. 9. It can be seen that the temperature measurement stabilises for large portions removed, indicating that the central BEC is no longer affecting the measurement and we are indeed in the thermal region. This process is similar to the one employed in Ref. [39].

While the momentum profile appears normal we need to account for the interactions between the species. Using the numerical method described in Ref. [68] we can find the expected position and momentum distribution of an interacting bose-fermi mixture at a finite temperature T in a given trapping potential. For our experimental parameters we find a shift in apparent temperature of roughly 10 nK for both the Fermi and thermal Bose distributions, though this effect diminishes and eventually approaches zero with higher momenta. To account for this affect we incorporate a 10 nK uncertainty into our error budget of the temperature measurement.

Note that to separate the two species on the detector, we apply a linear magnetic gradient for a brief period of time. This shifts the momentum center of both clouds from zero to some separate finite value. This hence modifies the equations in Tab. I by an effective change in t_0, which equals the time at which center-of-momentum of the cloud hits the detector.

[1] M. H. Anderson, J. R. Ensher, M. R. Matthews, C. E. Wieman, and E. A. Cornell, Observation of bose-einstein condensation in a dilute atomic vapor, science **269**, 198 (1995).

[2] T. Jeltes, J. M. McNamara, W. Hogervorst, W. Vassen, V. Krachmalnicoff, M. Schellekens, A. Perrin, H. Chang, D. Boiron, A. Aspect, and C. I. Westbrook, Comparison of the Hanbury Brown-Twiss effect for bosons and fermions, Nature **445**, 402 (2007).

[3] A. G. Manning, R. I. Khakimov, R. G. Dall, and A. G. Truscott, Wheeler's delayed-choice gedanken experiment with a single atom, Nature Physics **11**, 539 (2015).

[4] R. Lopes, A. Imanaliev, A. Aspect, M. Cheneau, D. Boiron, and C. I. Westbrook, Atomic Hong–Ou–Mandel experiment, Nature **520**, 66 (2015).

[5] A. G. Manning, S. S. Hodgman, R. G. Dall, M. T. Johnsson, and A. G. Truscott, The Hanbury Brown-Twiss effect in a pulsed atom laser, Opt. Express **18**, 18712 (2010).

[6] P. Dussarrat, M. Perrier, A. Imanaliev, R. Lopes, A. Aspect, M. Cheneau, D. Boiron, and C. I. Westbrook, Two-Particle Four-Mode Interferometer for Atoms, Phys. Rev. Lett. **119**, 173202 (2017).

[7] D. K. Shin, B. M. Henson, S. S. Hodgman, T. Wasak, J. Chwedeńczuk, and A. G. Truscott, Bell correlations between spatially separated pairs of atoms, Nature Communications **10** (2019).

[8] M. Bonneau, W. J. Munro, K. Nemoto, and J. Schmiedmayer, Characterizing twin-particle entanglement in double-well potentials, Phys. Rev. A **98**, 033608 (2018).

[9] F. Borselli, M. Maiwöger, T. Zhang, P. Haslinger, V. Mukherjee, A. Negretti, S. Montangero, T. Calarco, I. Mazets, M. Bonneau, and J. Schmiedmayer, Two-Particle Interference with Double Twin-Atom Beams, Phys. Rev. Lett. **126**, 083603 (2021).

[10] B. M. Henson, J. A. Ross, K. F. Thomas, C. N. Kuhn, D. K. Shin, S. S. Hodgman, Y.-H. Zhang, L.-Y. Tang, G. W. F. Drake, A. T. Bondy, A. G. Truscott, and K. G. H. Baldwin, Measurement of a helium tune-out frequency: an independent test of quantum electrodynamics, Science **376**, 199 (2022), https://www.science.org/doi/pdf/10.1126/science.abk2502.

[11] T. Byrnes, K. Wen, and Y. Yamamoto, Macroscopic quantum computation using bose-einstein condensates, Phys. Rev. A **85**, 040306 (2012).

[12] T. Byrnes, D. Rosseau, M. Khosla, A. Pyrkov, A. Thomasen, T. Mukai, S. Koyama, A. Abdelrahman, and E. Ilo-Okeke, Macroscopic quantum information processing using spin coherent states, Optics Communications **337**, 102 (2015), macroscopic quantumness: theory and applications in optical sciences.

[13] P. A. Murthy, M. Neidig, R. Klemt, L. Bayha,

Statistics	In-trap Momentum Distribution	$n^{tof}(t)$	$n^{tof}(x)$
Bose-Einstein	$A_b\,\mathrm{Li}_{\frac{3}{2}}\left[\xi_b\exp\left(-\frac{p^2}{m_b^2 v_f^2}\right)\right]$	$\pi m_b^3 A_b v_0^2 g_0\left(1+\frac{t_0^2}{t^2}\right)\mathrm{Li}_{\frac{5}{2}}\left[\xi_b g(t)\right]$	$\pi m_b^3 A_b\frac{v_0^2}{t_0}\mathrm{Li}_{\frac{5}{2}}\left[\xi_b f(x)\right]$
Fermi-Dirac	$-A_f\,\mathrm{Li}_{\frac{3}{2}}\left[-\xi_f\exp\left(-\frac{p^2}{m_f^2 v_b^2}\right)\right]$	$-\pi m_f^3 A_f v_0^2 g_0\left(1+\frac{t_0^2}{t^2}\right)\mathrm{Li}_{\frac{5}{2}}\left[-\xi_f g(t)\right]$	$-\pi m_f^3 A_f\frac{v_0^2}{t_0}\mathrm{Li}_{\frac{5}{2}}\left[-\xi_f f(x)\right]$
Maxwell-Boltzmann	$A_t e^{-\frac{p^2}{m^2 v_0^2}}$	$\pi m_f^3 A_t v_0^2 g_0\left(1+\frac{t_0^2}{t^2}\right)g(t)$	$\pi A_t m_f^3\frac{v_0^2}{t_0}f(x)$
Bose-Einstein Condensate	-	$\lambda A_{bec} t^2\left[1-\left(\frac{g_0(t^2-t_0^2)}{2R(t)}\right)^2\right]$	$A_{bec} t_0^2\left[1-\left(\frac{x}{\lambda R(t_0)}\right)^2\right]$

TABLE I. Summary of the momentum and time-of-flight profiles for different particle statistics and a Bose-Einstein condensate. In the above we have used the following abbreviations: p is the magnitude of the three dimensional momentum vector; $v_{b,f}=\left(\frac{2k_B T}{m_{b,f}}\right)^{1/2}$ is the most probable velocity of the fermions and bosons respectively; $A_{b,f}=\frac{1}{(2\pi)^{3/2}\hbar^3}\left(\frac{k_B T}{m_{b,f}\bar\omega_{b,f}^2}\right)^{3/2}$, $A_t=\frac{N_t}{(2\pi)^{3/2}(mk_B T)^{3/2}}$, and $A_{bec}=\frac{\pi\mu_b^2}{m_b}$ are the normalisation constants of the respective momentum distributions; $\xi_{f,b}=e^{\frac{-\mu_{f,b}}{k_B T}}$ is the faugacity of the respective distribution; $\lambda=\frac{\pi\omega_x}{2\omega_{z,y}}$ is the aspect ratio of the time-of-flight profile of the BEC; $R(t)=\sqrt{\frac{2\mu_b}{m_b}}t$; $g(t)=\exp\left(-\frac{g_0(t^2-t_0^2)^2}{2v_{0,f}^2 t^2}\right)$; $f(x)=\exp\left(-\frac{x^2}{v_0^2 t_0^2}\right)$. These distributions are all valid for $v_{f,b}t_0\ll l_0$. This is equivalent to assuming the average expansion of the cloud is negligible compared to the fall distance, which for our experiment is a very good approximation. We use the semi-classical approach and assume the behaviour of an ideal gas for all distributions except the BEC. For the BEC the mean-field energy dominates and we use the scaling solution derived in Ref. [43].
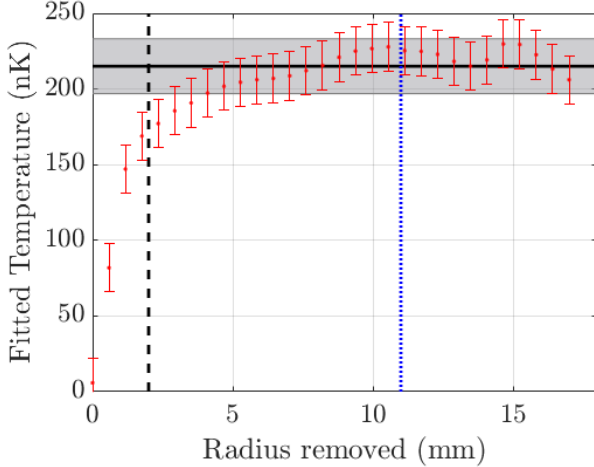

FIG. 9. Fitted temperature versus removed fraction, for the same data presented in Fig. 5. The removed fraction is measured by the radius from the average position, center, of the cloud. The BEC has a radius on the detector of 2 mm, shown as a black dashed line. The final measured temperature corresponds to a thermal width (standard deviation) of 11 mm on the detector. Thus the width of the thermal cloud is much larger than that of the BEC, as required for a good fit. The final measured temperature of 215(18) nK is shown as a horizontal black line, with gray shaded region indicating the uncertainty. It can be seen that the measured temperature rapidly converges onto the measured value from removed fractions larger than the BEC radius.

I. Boettcher, T. Enss, M. Holten, G. Zürn, P. M. Preiss, and S. Jochim, High-temperature pairing in a strongly interacting two-dimensional fermi gas, Science **359**, 452 (2018).

[14] M. W. Zwierlein, J. R. Abo-Shaeer, A. Schirotzek, C. H. Schunck, and W. Ketterle, Vortices and superfluidity in a strongly interacting fermi gas, Nature **435**, 1047 (2005).

[15] J. K. Chin, D. Miller, Y. Liu, C. Stan, W. Setiawan, C. Sanner, K. Xu, and W. Ketterle, Evidence for superfluidity of ultracold fermions in an optical lattice, Nature **443**, 961 (2006).

[16] B. DeMarco and D. S. Jin, Onset of fermi degeneracy in a trapped atomic gas, Science **285**, 1703 (1999), https://www.science.org/doi/pdf/10.1126/science.285.5434.1703.

[17] I. Bloch, J. Dalibard, and W. Zwerger, Many-body physics with ultracold gases, Rev. Mod. Phys. **80**, 885 (2008).

[18] S. Giorgini, L. P. Pitaevskii, and S. Stringari, Theory of ultracold atomic fermi gases, Rev. Mod. Phys. **80**, 1215 (2008).

[19] F. M. Marchetti, C. J. M. Mathy, D. A. Huse, and M. M. Parish, Phase separation and collapse in bose-fermi mixtures with a feshbach resonance, Phys. Rev. B **78**, 134517 (2008).

[20] S. G. Bhongale and H. Pu, Phase separation in a mixture of a bose-einstein condensate and a two-component fermi gas as a probe of fermi superfluidity, Phys. Rev. A **78**, 061606 (2008).

[21] J. Linder and A. Sudbø, Probing phase separation in bose-fermi mixtures by the critical superfluid velocity, Phys. Rev. A **81**, 013622 (2010).

[22] D. Rakshit, T. Karpiuk, M. Brewczyk, and M. Gajda, Quantum Bose-Fermi droplets, SciPost Phys. **6**, 79 (2019).

[23] J.-B. Wang, J.-S. Pan, X. Cui, and W. Yi, Quantum droplets in a mixture of bose–fermi superfluids, Chinese Physics Letters **37**, 076701 (2020).

[24] C. Kohstall, M. Zaccanti, M. Jag, A. Trenkwalder, P. Massignan, G. M. Bruun, F. Schreck, and R. Grimm, Metastability and coherence of repulsive polarons in a strongly interacting fermi mixture, Nature **485**, 615 (2012).

[25] C.-H. Wu, I. Santiago, J. W. Park, P. Ahmadi, and M. W. Zwierlein, Strongly interacting isotopic bose-fermi mixture immersed in a fermi sea, Phys. Rev. A **84**, 011601 (2011).

[26] I. Fritsche, C. Baroni, E. Dobler, E. Kirilov, B. Huang, R. Grimm, G. M. Bruun, and P. Massignan, Stability and breakdown of fermi polarons in a strongly interacting fermi-bose mixture, Phys. Rev. A **103**, 053314 (2021).

[27] F. Scazza, M. Zaccanti, P. Massignan, M. M. Parish, and J. Levinsen, Repulsive fermi and bose polarons in quantum gases, Atoms **10**, 10.3390/atoms10020055 (2022).

[28] M. K. Tey, S. Stellmer, R. Grimm, and F. Schreck, Double-degenerate bose-fermi mixture of strontium, Phys. Rev. A **82**, 011608 (2010).

[29] J. W. Park, C.-H. Wu, I. Santiago, T. G. Tiecke, S. Will, P. Ahmadi, and M. W. Zwierlein, Quantum degenerate bose-fermi mixture of chemically different atomic species with widely tunable interactions, Phys. Rev. A **85**, 051602 (2012).

[30] K. Günter, T. Stöferle, H. Moritz, M. Köhl, and T. Esslinger, Bose-fermi mixtures in a three-dimensional optical lattice, Phys. Rev. Lett. **96**, 180402 (2006).

[31] C. Ospelkaus, S. Ospelkaus, K. Sengstock, and K. Bongs, Interaction-driven dynamics of ^{40}K$-^{87}$Rb fermion-boson gas mixtures in the large-particle-number limit, Phys. Rev. Lett. **96**, 020401 (2006).

[32] G. Roati, F. Riboli, G. Modugno, and M. Inguscio, Fermi-bose quantum degenerate ^{40}K$-^{87}$Rb mixture with attractive interaction, Phys. Rev. Lett. **89**, 150403 (2002).

[33] T. Sowiński and M. Á. García-March, One-dimensional mixtures of several ultracold atoms: a review, Reports on Progress in Physics **82**, 104401 (2019).

[34] R. Onofrio, Cooling and thermometry of atomic fermi gases, Physics-Uspekhi **59**, 1129 (2016).

[35] G. Modugno, G. Roati, F. Riboli, F. Ferlaino, R. J. Brecha, and M. Inguscio, Collapse of a degenerate fermi gas, Science **297**, 2240 (2002), https://www.science.org/doi/pdf/10.1126/science.1077386.

[36] A. G. Truscott, K. E. Strecker, W. I. McAlexander, G. B. Partridge, and R. G. Hulet, Observation of fermi pressure in a gas of trapped atoms, Science **291**, 2570 (2001), https://www.science.org/doi/pdf/10.1126/science.1059318.

[37] F. Schreck, G. Ferrari, K. L. Corwin, J. Cubizolles, L. Khaykovich, M.-O. Mewes, and C. Salomon, Sympathetic cooling of bosonic and fermionic lithium gases towards quantum degeneracy, Phys. Rev. A **64**, 011402 (2001).

[38] S. Aubin, S. Myrskog, M. H. T. Extavour, L. J. LeBlanc, D. McKay, A. Stummer, and J. H. Thywissen, Rapid sympathetic cooling to fermi degeneracy on a chip, Nature Physics **2**, 384 (2006).

[39] J. M. McNamara, T. Jeltes, A. S. Tychkov, W. Hogervorst, and W. Vassen, Degenerate bose-fermi mixture of metastable atoms, Phys. Rev. Lett. **97**, 080404 (2006).

[40] R. Dall and A. Truscott, Bose–Einstein condensation of metastable helium in a bi-planar quadrupole Ioffe configuration trap, Opt. Commun. **270**, 255 (2007).

[41] C. J. Pethick and H. Smith, *Bose–Einstein condensation in dilute gases* (Cambridge university press, 2008).

[42] S. Moal, M. Portier, J. Kim, J. Dugué, U. D. Rapol, M. Leduc, and C. Cohen-Tannoudji, Accurate determination of the scattering length of metastable helium atoms using dark resonances between atoms and exotic molecules, Phys. Rev. Lett. **96**, 023203 (2006).

[43] Y. Castin and R. Dum, Bose-einstein condensates in time dependent traps, Phys. Rev. Lett. **77**, 5315 (1996).

[44] G. Baym and C. J. Pethick, Ground-state properties of magnetically trapped bose-condensed rubidium gas, Phys. Rev. Lett. **76**, 6 (1996).

[45] D. A. Butts and D. S. Rokhsar, Trapped fermi gases, Phys. Rev. A **55**, 4346 (1997).

[46] B. L. DeMarco, *Quantum behavior of an atomic Fermi gas* (University of Colorado at Boulder, 2001).

[47] I. Yavin, M. Weel, A. Andreyuk, and A. Kumarakrishnan, A calculation of the time-of-flight distribution of trapped atoms, American Journal of Physics **70**, 149 (2002).

[48] H. J. Metcalf and P. Van der Straten, Laser cooling and trapping (Springer-Verlag, New York, 1999) Chap. 4, pp. 53–56.

[49] S. S. Hodgman, R. G. Dall, L. J. Byron, K. G. H. Baldwin, S. J. Buckman, and A. G. Truscott, Metastable helium: A new determination of the longest atomic excited-state lifetime, Phys. Rev. Lett. **103**, 053002 (2009).

[50] J. Swansson, K. Baldwin, M. Hoogerland, A. Truscott, and S. Buckman, A high flux, liquid-helium cooled source of metastable rare gas atoms, Applied Physics B **79**, 485 (2004).

[51] T. Jeltes, *Quantum Statistical Effects in Ultracold Gases of Metastable Helium*, Ph.D. thesis, Vrije Universiteit Amsterdam (2008).

[52] A. Kramida, Y. Ralchenko, J. Reader, and NIST ASD Team, (2019), NIST Atomic Spectra Database (ver. 5.7.1), [Online]. Available: https://physics.nist.gov/asd [2019, November 10]. National Institute of Standards and Technology, Gaithersburg, MD.

[53] P. C. Pastor, G. Giusfredi, P. D. Natale, G. Hagel, C. de Mauro, and M. Inguscio, Absolute frequency measurements of the $2^3S_1 \rightarrow 2^3P_{0,1,2}$ atomic helium transitions around 1083 nm, Phys. Rev. Lett. **92**, 023001 (2004).

[54] J. D. Prestage, C. E. Johnson, E. A. Hinds, and F. M. J. Pichanick, Precise study of hyperfine structure in the 2^3p state of ^{3}He, Phys. Rev. A **32**, 2712 (1985).

[55] W. Vassen, C. Cohen-Tannoudji, M. Leduc, D. Boiron, C. I. Westbrook, A. Truscott, K. Baldwin, G. Birkl, P. Cancio, and M. Trippenbach, Cold and trapped metastable noble gases, Rev. Mod. Phys. **84**, 175 (2012).

[56] R. J. W. Stas, *Trapping fermionic and bosonic helium atoms*, Ph.D. thesis, Vrije Universiteit Amsterdam (2005).

[57] W. Geist, A. Idrizbegovic, M. Marinescu, T. A. B. Kennedy, and L. You, Evaporative cooling of trapped fermionic atoms, Phys. Rev. A **61**, 013406 (1999).

[58] L. D. Carr and Y. Castin, Limits of sympathetic cooling of fermions: The role of heat capacity of the coolant, Phys. Rev. A **69**, 043611 (2004).

[59] Assuming the phase space density of the mixture and the efficiency of the evaporation cycle both remain constant for T greater than T_C the exact functional form is given by $K = \frac{1}{f(\eta)} \left(\frac{S_f(\tau, N_f)}{k_b N_f} + 6\zeta(4) \left(\frac{\bar{\omega}_f}{\bar{\omega}_b} \right)^3 \tau \right) - \frac{N_b}{N_f}$ where K is a constant of motion, τ is the reduced temperature, $f(\eta)$ is the average energy of an boson with energy greater

than or equal to $\eta k_b T$, $\frac{S_f(\tau, N_f)}{k_b N_f}$ is the reduced entropy of a fermi gas (which purely a function of τ). The initial assumption essentially fixes K and η, and is hence why we can apply the equation to a range of initial conditions and evaporation heights. The previous equation is only strictly valid for temperatures less than T_C.

[60] B. M. Henson, K. F. Thomas, Z. Mehdi, T. G. Burnett, J. A. Ross, S. S. Hodgman, and A. G. Truscott, Trap frequency measurement with a pulsed atom laser, Opt. Express **30**, 13252 (2022).

[61] R. C. Hilborn, Einstein coefficients, cross sections, f values, dipole moments, and all that, American Journal of Physics **50**, 982 (1982), https://doi.org/10.1119/1.12937.

[62] D. K. Shin, B. M. Henson, R. I. Khakimov, J. A. Ross, C. J. Dedman, S. S. Hodgman, K. G. H. Baldwin, and A. G. Truscott, Widely tunable, narrow linewidth external-cavity gain chip laser for spectroscopy between 1.0 - 1.1 μm, Opt. Express **24**, 27403 (2016).

[63] D. J. Thompson and R. E. Scholten, Narrow linewidth tunable external cavity diode laser using wide bandwidth filter, Review of Scientific Instruments **83**, 023107 (2012).

[64] T. Okoshi, K. Kikuchi, and A. Nakayama, Novel method for high resolution measurement of laser output spectrum, Electron. Lett. **16**, 630 – 631 (1980).

[65] A. G. Manning, W. RuGway, S. S. Hodgman, R. G. Dall, K. G. H. Baldwin, and A. G. Truscott, Third-order spatial correlations for ultracold atoms, New Journal of Physics **15**, 013042 (2013).

[66] R. G. Dall, A. G. Manning, S. S. Hodgman, W. RuGway, K. V. Kheruntsyan, and A. G. Truscott, Ideal n-body correlations with massive particles, Nature Physics **9**, 341 (2013).

[67] R. Geiger and M. Trupke, Proposal for a quantum test of the weak equivalence principle with entangled atomic species, Phys. Rev. Lett. **120**, 043602 (2018).

[68] Z. Akdeniz, A. Minguzzi, P. Vignolo, and M. P. Tosi, Demixing in mesoscopic boson-fermion clouds inside cylindrical harmonic traps: Quantum phase diagram and role of temperature, Phys. Rev. A **66**, 013620 (2002).